Petroleum Science 21 (2024) 4481–4496

Contents lists available at ScienceDirect

Petroleum Science

journal homepage: www.keaipublishing.com/en/journals/petroleum-science

Original Paper

Characterization of oxygen initiation process in the autothermic pyrolysis in-situ conversion of Huadian oil shale

Shao-Tao Xu [a], Xiao-Shu Lü [b, e, f], Han Wang [b, d, **], You-Hong Sun [a, b, c, d, ***], Shi-Jie Kang [g], Zhen-Dong Wang [h], Wei Guo [b, c, d], Sun-Hua Deng [b, c, *]

[a] School of Engineering and Technology, China University of Geosciences, Beijing, 100083, China
[b] College of Construction Engineering, Jilin University, Changchun, 130021, Jilin, China
[c] National-Local Joint Engineering Laboratory of In-situ Conversion, Drilling and Exploitation Technology for Oil Shale, Jilin University, Changchun, 130021, Jilin, China
[d] Key Lab of Ministry of Natural Resources for Drilling and Exploitation Technology in Complex Conditions, Jilin University, Changchun, 130021, Jilin, China
[e] Department of Electrical Engineering and Energy Technology, University of Vaasa, P.O.Box 700, FIN-65101, Vaasa, Finland
[f] Department of Civil and Structural Engineering, School of Engineering, Aalto University, PO Box 12100, FIN-02015, Espoo, Finland
[g] Ganjiang Innovation Academy, Chinese Academy of Sciences, Ganzhou, 341000, Jiangxi, China
[h] Key Laboratory of Coal Exploration and Comprehensive Utilization, Ministry of Nature and Resources, Shaanxi Coal Geology Group Co., Ltd., Xi'an, 710021, Shaanxi, China

ARTICLE INFO

Article history:
Received 8 January 2024
Received in revised form
23 July 2024
Accepted 24 July 2024
Available online 26 July 2024

Edited by Min Li

Keywords:
Oil shale
Oxygen initiation process
Isothermal kinetic analysis
Heat release
Product release characteristics

ABSTRACT

The oxygen initiation process, one of the key processes in the early stage of the autothermic pyrolysis in-situ conversion technology, has not been deeply investigated, which seriously limits its development. In this study, the reaction behaviors, kinetic parameters, heat and product release characteristics during the isothermal oxygen initiation process of Huadian oil shale in O_2/N_2 mixtures with different oxygen concentrations and initiation temperatures were investigated via TG/DSC-FTIR. The results show that the samples exhibit three different reaction behaviors during the initiation stage, consisting of two main parts, i.e., the oxidative weight-gain and the oxidative reaction phases. The former phase is mainly characterized by the oxygen addition reaction that produces oxidizing groups which increase the sample mass. And the latter stage consists of two main subreactions. The first subreaction involves the oxidative cracking and pyrolysis of oxidizing groups and kerogen to produce fuel deposits such as residual carbon, while the second subreaction focuses on the oxidation of the resulting fuels. Furthermore, increasing the oxygen concentration significantly promotes the above reactions, leading to an increase in the reaction intensity and reaction rate. Owing to the combined effect of oxygen concentration and residual organic matter content, the total heat release increases with the increasing initiation temperature and reaches its maximum at 330–370 °C. In addition, the preheating stage primarily produces hydrocarbon gases, while the initiation stage predominantly generates CO_2. As the preheating temperature increases, the CO_2 output intensifies, the required reaction time shortens, and the release becomes more concentrated. Based on these findings, a reaction mechanism for the oxygen initiation process of Huadian oil shale was proposed, and recommendations were provided for optimizing the construction process.

1. Introduction

Due to the increasing demand for energy and the gradual decline of conventional fossil resources, there is a growing emphasis on exploitation of unconventional energy sources (Hrayshat, 2008; Raul, 2018; Jarosław et al., 2021). Among these, oil shale (OS) is a kind of unconventional fossil resource with wide distributions and huge reserves worldwide (Kuang et al., 2019;

* Corresponding author.
** Corresponding author.
*** Corresponding author.
E-mail addresses: 13154374836@163.com (H. Wang), syh@cugb.edu.cn (Y.-H. Sun), denghua13@163.com (S.-H. Deng).

https://doi.org/10.1016/j.petsci.2024.07.024

Amer et al., 2022; Kang et al., 2023). Inside OS, large molecules of organic matter, called kerogen, are dispersed in nanoscale particles in a skeleton of inorganic minerals (Saif et al., 2017; Zhan et al., 2022). These large molecules of kerogen basically cannot be extracted by organic solvents but can be converted into liquid shale oil and gaseous shale gas when heated to 300–550 °C (Kang et al., 2021; Li et al., 2022). This liquid shale oil has extremely similar properties to conventional petroleum, making it a versatile alternative suitable for various application fields such as energy, chemicals, and materials (Sun et al., 2014, 2019). Moreover, OS deposits are found in 33 countries with an estimated resource of 411 billion tons of shale oil, equivalent to 2.9 trillion U.S. barrels of shale oil (Dyni, 2006; Liu et al., 2017). This substantial reserve holds exceptional potential for extraction over a considerable period of time. As a result, OS is currently attracting worldwide attention as a substitute resource for petroleum (Zhu et al., 2022).

The extraction of oil and gas from OS is mainly achieved by heating, and the existing technologies can be divided into two categories: surface retorting and in-situ conversion, according to their technical characteristics (Kang et al., 2020; Sun et al., 2021a). Surface retorting requires the OS to be mined to the surface and then heated to obtain hydrocarbons, which will form an underground empty area, produce massive residue accumulation on the surface, and emit enormous waste gas, which has the disadvantages of environmental damage and high cost. While in-situ conversion technology involves the extraction of shale oil and gas by directly heating OS reservoirs underground without mining operations (Xu et al., 2023). Therefore, it offers many advantages, including environmental friendliness, low cost, and wide applicability, which has presently become the prevailing direction for the development of OS exploitation (He et al., 2021; Huang et al., 2023). In recent years, more than a dozen in-situ conversion technologies for OS have been proposed successively, accompanied by theoretical and experimental studies (Song et al., 2019). However, most of these are costly and inefficient due to the complex equipment and massive energy injection (Kang et al., 2020; Shi et al., 2023). Furthermore, most of the above technologies remain at the laboratory research stage without subsequent in-situ pilot experiments (Wang et al., 2022).

In recent years, in-situ conversion technologies that utilize oxygen to assist OS exploitation are expected to overcome these limitations (Yang et al., 2022). The potential heat in the residue can be released by initiating oxidative reactions between oxygen and part of organic matter or residual carbon by-products formed during pyrolysis (Guo et al., 2016a). This heat can then be used to assist in heating the OS, thus significantly reducing the energy input and increasing the production efficiency (Guo et al., 2022b). Based on the above theory, considerable in-situ conversion methods and strategies have been proposed and studied, such as the co-current combustion method (Martins et al., 2010a, 2010b), self-heating retorting (Guo et al., 2013, 2016b), oxidative assisted pyrolysis (Xu et al., 2023b), co-current oxidizing pyrolysis (Guo et al., 2020, 2021), and in-situ combustion technique (Bolotov et al., 2023). These methods have been widely investigated in laboratory experiments, which demonstrate that oxygen can assist in the pyrolysis of OS at a lower external energy input to obtain higher oil yields and improved oil quality. However, field experiments haven't been conducted, and the feasibility of actual production has not been verified. Lately, an autothermic pyrolysis in-situ conversion (ATS) technology, one of the in-situ conversion technologies for OS that utilizes oxygen, was successfully field-piloted in Fuyu, Jilin Province, China, and significant quantities of shale oil and gas were recovered (Guo et al., 2022a). This accomplishment not only proves the theoretical feasibility and operational viability of ATS, but also demonstrates the effective application of oxygen in OS exploitation.

Specifically, the ATS technology involves three stages: the preheating stage, the initiation stage, and the reaction stage (Xu et al., 2023a). In the preheating stage, the OS is preheated in nitrogen to reach a target temperature of T_0. Subsequently, the injected gas is switched to air for initiating oxidative exothermic reactions, which is the initiation stage. When the heat released by the oxidation reactions meets the requirement for in-situ OS pyrolysis, the underground chain reaction can occur continuously without external energy input. Thereby, the oil and gas products can achieve self-production in the reaction stage, significantly reducing costs (Xu et al., 2023c). The transition from the preheating stage to the initiation stage, characterized by substantial and complex chemical reactions and heat release between organic matter and oxygen, is called the oxygen initiation process (OIP). It is one of the foundations and keys of the ATS technology. Previous studies have demonstrated that nitrogen-to-air switching is a remarkably effective OIP strategy that can significantly increase oil yields and reduce external energy input (Sun et al., 2021b; Xu et al., 2021). For example, preheating the OS under hypoxic conditions to 370 °C followed by switching to oxygen could obtain an oil yield equivalent to more than 90% of Fischer assay results (obtained at 520 °C) (Guo et al., 2020). In contrast, the oil yield was obviously reduced when air was used throughout the experiment (Guo et al., 2013). This is attributed to the fact that the switch of nitrogen-to-air dramatically increases the heat generation and release rates, promoting residual carbon generation and oxidation exotherm, thus enabling the chain reactions to continue efficiently (Guo et al., 2015a, 2015b). As a result, it is necessary to deeply investigate the reaction behavior and mechanism in the nitrogen-to-air switching of the OS ATS technology to deepen the understanding for OIP.

So far, numerous researchers have conducted investigations into the reaction characteristics and kinetics of OS in different atmospheres, including pyrolysis under inert gases and oxidation reactions in oxygenated gases. The commonly used research methods and theories include thermogravimetric (TG) experiments, infrared analysis, and kinetic analysis (Bai et al., 2015a, 2020a; He et al., 2020). The results show that particle size, heating rate, and specimen mass exhibit significant correlations with the pyrolysis behavior of Huadian OS. Among them, heating rate has a significant effect on both product release and average activation energy, whereas particle size has the least effect on product release and specimen mass has the least effect on average activation energy (Mohammad et al., 2011; Bai et al., 2020b; Pan et al., 2021). Pyrolysis of bitumen under air exhibits three main reaction stages, namely low temperature oxidation (LTO), fuel deposition (FD), and high temperature oxidation (HTO), while the thermo-oxidative decomposition of kerogen has two main stages, FD and HTO. Three types of reactions are involved in LTO, i.e., oxygen addition reaction, decomposition, and isomerization. In addition, evaporation of hydrocarbons plays a significant role in the mass loss of the LTO stage. Isomerization and decomposition of bitumen, kerogen pyrolysis, and oxidative cracking reactions all occur mainly in the FD stage, generating large amounts of coke. And coke combustion is recognized to dominate in HTO (Yuan et al., 2018, 2022; Ifticene et al., 2022). Moreover, both branched and straight-chain alkanes exhibit only LTO and contribute little to coke formation (Yuan et al., 2019). The kinetic analysis results show that a 30% O_2/70% CO_2 environment is optimal for OS combustion, and the combustion process includes multiple reaction stages (Bai et al., 2015b, 2019). Furthermore, the various organic components and inorganic minerals have a large impact on the pyrolysis behavior and kinetic properties of OS (Wang et al., 2021; Yang et al., 2021).

Although considerable relevant research has been conducted and reported, there are still some gaps between the research

findings and the actual situation in the ATS technology. For example, the above researches were all performed in a single atmosphere under non-isothermal conditions. While in the ATS technology, the OIP is carried out by preheating the OS to the target temperature in nitrogen and then injecting air for oxygen initiation. This process involves the switching of nitrogen to oxygen-containing gas and is initiated and maintained at a constant target temperature. Thus, the effect of atmospheric switching on the reaction process of OS has not been conclusively determined. In addition, the potentially optimal oxygen concentration for the OIP is still unknown. Above all, it is necessary to conduct systematic investigations under variable atmospheres and isothermal conditions in order to identify the reaction characteristics of OIP.

In this study, a series of isothermal TG experiments, which allowed for atmosphere switching at different stages, were designed and conducted to investigate the reaction behavior and product release characteristics of the OS OIP at different temperatures and various oxygen concentrations by employing the TG/DSC-FTIR technique. Meanwhile, an isothermal kinetic model was used to calculate the kinetic parameters at initiation stage. Based on the results, a reaction mechanism of OS in the OIP at different temperatures was proposed. This research aims to complement the theoretical basis and deepen the understanding of the OIP of the OS ATS technology.

2. Material and methods

2.1. Material

The raw OS used in this study was obtained from Huadian, Jilin Province, China. Table 1 shows the results of proximate, ultimate, and Fischer assay analyses of the sample. These tests were performed in triplicate, with the average value being used. The raw OS was crushed and screened to 0.4–1.7-mm-sized particles, and subsequently dried in the oven at 80 °C for 10 h before initiating the experiment.

2.2. Analytical methods

2.2.1. TG analysis

TG and differential scanning calorimetry (DSC) analyses were performed using an STA 449F3 thermal analyzer (Netzsch, Germany). Nitrogen was the protective gas with a flow rate of 20 mL/min, while N_2 and O_2/N_2 mixtures with different oxygen concentrations (10, 21, 30, 50, and 100%) were the carrier gases with 80 mL/min. A 20 mg (±0.5 mg) powder sample was used in each test to reduce the influence of temperature gradients and heat and mass transfer effects. After that, each TG/DSC experiment consists of two stages, namely, the preheating stage in N_2 and the initiation stage in O_2/N_2 mixtures.

It should be noted that due to the limitations of the instrument, when heating to the target temperature at the heating rate of 10 °C/min, the temperature actually reached will exceed the set temperature. This phenomenon is called “overshoot”, which is more obvious at low temperatures. Therefore, in order to reduce overshoot, a two-step heating procedure was adopted in the preheating stage to extend the heating time. As shown in Fig. 1, the sample was first heated from 30 °C to (T_0−10) °C at a heating rate of 10 °C/min in N_2. Then, the sample was heated from (T_0−10) °C to T_0 °C at a heating rate of 1 °C/min. With this two-step heating, the OS samples could reach the initiation temperature of T_0 °C (170, 190, …, 290, 330, …, 450, and 520 °C) without obvious overshoot in the preheating stage. Next, N_2 was switched to the O_2/N_2 mixture to enter the initiation stage. In the initiation stage, the ambient temperature was maintained at T_0 for 2 h to make it undergo sufficient oxidation. After that, the whole TG/DSC experiment was completed. Exceptionally, the TG experiments in Fig. 2 were all performed in a single atmosphere (N_2 or air) at a heating rate of 10 °C/min from 30 to 900 °C. Duplicate experiments were performed to ensure reproducibility, and the errors in mass loss and temperature were less than 0.5 wt% and 1 °C, respectively.

2.2.2. FTIR analysis

The gaseous products were in-situ detected using a Thermo Scientific Nicolet iS10 FTIR spectrometer (America), which was coupled with the TG analyzer via a stainless-steel transfer pipe. The spectra were recorded at 4000–500 cm^{-1} with a resolution of 4 cm^{-1}. The stainless-steel transfer pipe and the gas cell in FTIR were kept at a constant temperature of 200 °C to minimize secondary reactions and ensure better transport.

Before TG/DSC and FTIR analysis, the OS sample was ground into fine powders and fully mixed to eliminate the heterogeneity of the sample. Moreover, multiple experiments were performed to ensure data reproducibility and accuracy.

3. Results and discussion

3.1. The reaction behaviors of OS at different stages

3.1.1. Pyrolysis and oxidation behaviors of OS

The TG/DTG curves of OS in N_2 and air are shown in Fig. 2. The TG/DTG curves can be divided into three stages. In stage I (<200 °C), the primary weight loss arises from the evaporation of free hydrocarbons and water, including interlayer and bound water of clay minerals; subsequently, the weight loss in stage II (200–600 °C) is mainly attributed to the pyrolysis of kerogen and oxidation of by-products such as residual carbon, which represents the main reaction interval of organic matter in OS; and stage III (>600 °C) primarily involves the decomposition of minerals, including carbonates and clay minerals, etc. (Xu et al., 2021, 2023a).

As displayed in Fig. 2, the thermal weight losses for the three stages in N_2 are 2.18%, 22.22%, and 7.33%, respectively, while those in air are 2.20%, 29.85%, and 4.94%. These results illustrate that the reactions of OS in these 2 atm are significantly different. In N_2, the kerogen was pyrolyzed in stage II, which liberated substantial amounts of hydrocarbon products (Guo et al., 2022b; Xu et al.,

Table 1
The proximate, ultimate, and Fischer assay analysis results of the raw Huadian OS.

Proximate analysis, wt.% (ad)		Sd	Ultimate analysis, wt.% (d)		Sd	Fischer assay analysis, wt.% (ad)		Sd
Moisture	4.26	0.09	C	22.20	0.15	Shale oil	14.91	0.07
Volatile matter	30.63	0.11	H	3.07	0.05	Water	5.57	0.04
Ash	61.79	0.12	N	0.50	0.03	Semi-coke	72.16	0.12
Fixed carbon	3.32	0.09	O	12.90	0.06	Gases + loss	7.36	0.08
Calorific value	9.82 MJ/kg							

Note: ad: air dried, d: dried, Sd: Standard deviation.

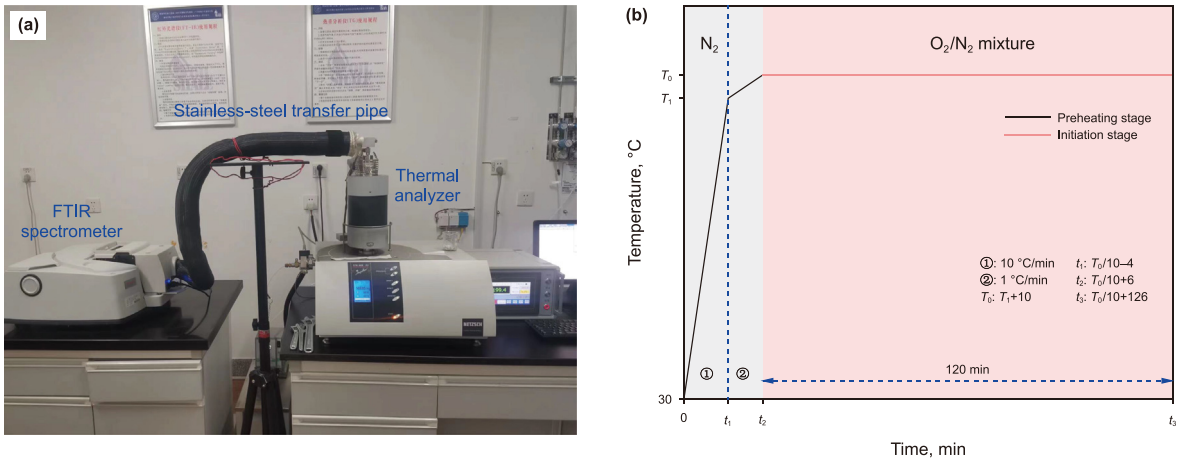

Fig. 1. **(a)** TG/DSC-FTIR experimental apparatus and **(b)** schematic diagram of temperature program for TG/DSC experiments of OS.

2023b). Simultaneously, considerable by-products, such as residual carbon and heavy bitumen, were also generated and remained in the OS matrix (Sun et al., 2019; Kang et al., 2021). However, in air, except for the release of pyrolytic hydrocarbon products, these remaining by-products reacted with oxygen, leading to an increase in weight loss (Xu et al., 2021; Yang et al., 2022). In addition, a significant amount of heat released by the oxidation reaction increased the internal temperature of OS, substantially exceeding the heating temperature (which could briefly reach over 700 °C when the ambient temperature is about 500 °C according to previous studies) (Guo et al., 2013; Xu et al., 2023c). Consequently, this led to the earlier decomposition of carbonate and clay minerals, ultimately causing increased weight loss in stage II and a decrease in stage III.

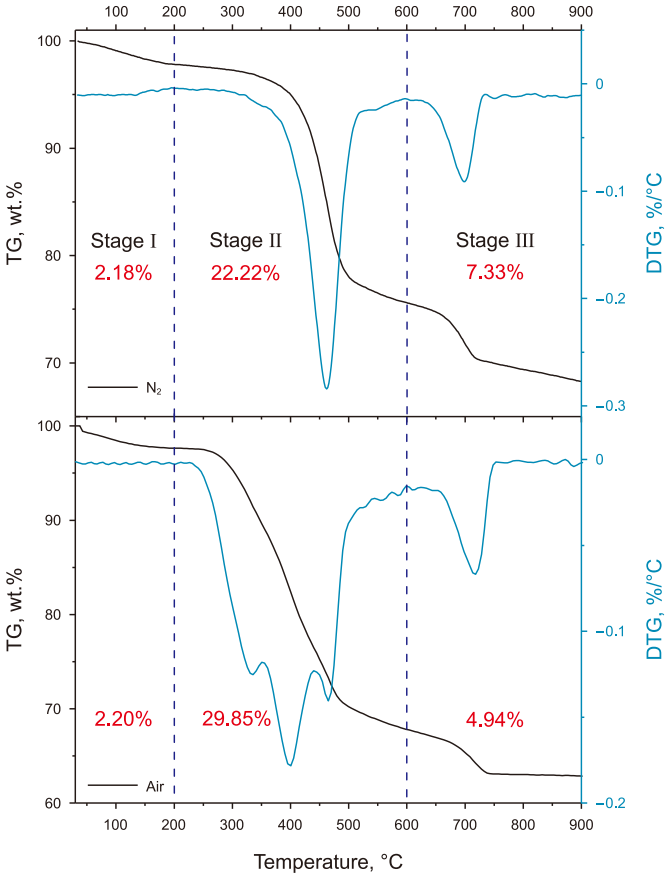

Fig. 2. TG/DTG curves of Huadian OS in N_2 and air.

3.1.2. OIP at different initiation temperatures

The TG curves for OS encompass two primary stages: the preheating and the initiation stage. Taking the case shown in Fig. 3(b) as an example, during the preheating stage, the OS sample was first preheated in N_2 for 31 min (t_2 in Fig. 1) to reach 250 °C. Subsequently, the carrier gas was switched from N_2 to a 21% O_2/79% N_2 mixture, maintaining a constant temperature for 120 min, thereby completing the initiation stage. The results indicate a gradual decrease in OS mass during the preheating stage. Then, a slight temporary weight-gain from M_0 to M_{max} is observed at the beginning of the initiation stage, followed by a continuous decrease. This suggests that at the initial period when oxygen was introduced, the reactive radicals in the free bitumen and kerogen first combined with oxygen to undergo oxygen addition reactions, generating oxidizing groups, and leading to a small temporary increase in the mass of the organic components (Ifticene et al., 2022). Subsequently, further oxidative cracking and pyrolysis of these oxidizing groups and kerogen resulted in the escape of gaseous products, leading to a continuous decrease.

Notably, Fig. 3(a) reveals substantially longer durations from M_0 to M_{max} and a notably reduced subsequent decrease at lower preheating temperatures. Conversely, at higher initiation temperatures (T_0) (Fig. 3(c)), the preliminary weight-gain is barely observed in the TG curve, with only a continuous decrease being evident. These demonstrate that high temperatures can accelerate the initial oxidation and subsequent cracking reactions in the initiation stage, facilitating a significant reduction in reaction time. If the time interval for the initial oxidation is shorter than the minimum recordable interval (0.5 min) of the TG apparatus, it becomes indiscernible. Moreover, when the initiation temperature reaches a sufficiently high level, the organic matter may ignite directly upon oxygen injection, leading to a violent combustion reaction and rapid sample mass decrease.

3.1.3. Pyrolysis behavior of OS at preheating stage

To investigate the pyrolysis behavior of OS, the weight loss and its first derivative in the preheating stage at different temperatures were calculated, as depicted in Fig. 4. The results show that the weight loss in the preheating stage remains relatively stable until 270 °C, with a maximum of 2.58%. This value slightly exceeds the

2.18% (Stage I in N_2) resulting in Fig. 2 due to the longer preheating period and slightly higher temperature. It indicates that before 270 °C, the weight loss in the preheating stage is primarily attributed to the evaporation of water and low-boiling hydrocarbons in small quantities. However, these start to evaporate faster after 270 °C, and the oil and gas products begin to yield faster at higher temperatures (>330 °C), thereby causing a significant increase in weight loss. From 270 to 490 °C, the weight loss in the preheating stage increases by 20.30%. Comparing with the weight loss in stage II under N_2 (22.22%), it is evident that when the preheating temperature reaches 490 °C, most of the volatile components in the sample have been produced.

3.1.4. Reaction behavior of OS at initiation stage

In order to investigate the reaction behavior of OS, the total weight losses during the initiation stage were calculated at different initiation temperatures with various oxygen concentrations, as shown in Fig. 5. The results demonstrate that at low temperatures (170–190 °C), the total weight loss of OS is negative, indicating an increase in mass. This suggests that at this temperature, the kerogen undergoes mainly an oxygen addition reaction. Partial reactive groups in the kerogen reacted with oxygen to form oxidized groups. The FTIR (Fig. 13) results show that there was almost no gaseous product generation or release at this point. This suggests that these oxidized groups can be stabilized at such low temperatures, resulting in a slight increase in sample mass. After that, the total weight loss basically exhibits an increasing trend from 210 to 370 °C. As the preheating temperature increases, the oxidized groups undergo further reactions such as decomposition and isomerization (Yuan et al., 2018; Ifticene et al., 2022). The bitumen produced during the preheating stage (>300 °C) and kerogen also gradually start pyrolysis and oxidative cracking, generating and releasing a large amount of gaseous products, which lead to an increasing total weight loss. Finally, due to the increasing amount of hydrocarbon product generated from the kerogen cracking during the preheating stage, the total amounts of residual organic matter in the samples decrease significantly when the temperature is higher than 370 °C. Although the increase in preheating temperature intensifies the cracking and oxidizing reactions of organic matter in the initiation stage, the total weight loss shows a decreasing trend due to the decrease in the total amount of residual organic matter.

As mentioned above, various instances of oxidative weight gain were observed during the initiation stage. Table 2 summarizes the maximum oxidative weight gain and the corresponding time experienced during the initiation stage. The maximum oxidative weight gain (ΔM) represents the difference between the maximum mass (M_{max}) and the initial mass (M_0) of the sample during the initiation stage, with ΔT denoting the corresponding time interval, as shown in Fig. 3(a). The results show that at low initiation temperatures (170–330 °C), the samples all experienced different degrees of oxidative weight gain during the initiation stage. With 10%, 21%, and 100% O_2 concentrations, ΔM initially increases and subsequently decreases with rising temperature, while ΔM displays a decreasing trend in 30% and 50% O_2 concentrations. Furthermore, ΔM exhibits an increasing trend with increasing oxygen concentration, whereas ΔT shows a decreasing trend.

After the oxidative weight gain, the sample mass starts to decrease continuously as the temperature rises and the reaction progresses. The times experienced for the weight loss ratio, a (sample weight loss vs. total weight loss), to reach 30%, 50%, and 90% during the initiation stage of various TG curves were summarized in Fig. 6, respectively. The results showed that with the increase in initiation temperature, the time experienced to reach the target weight loss ratio displays a rapid decreasing trend in the

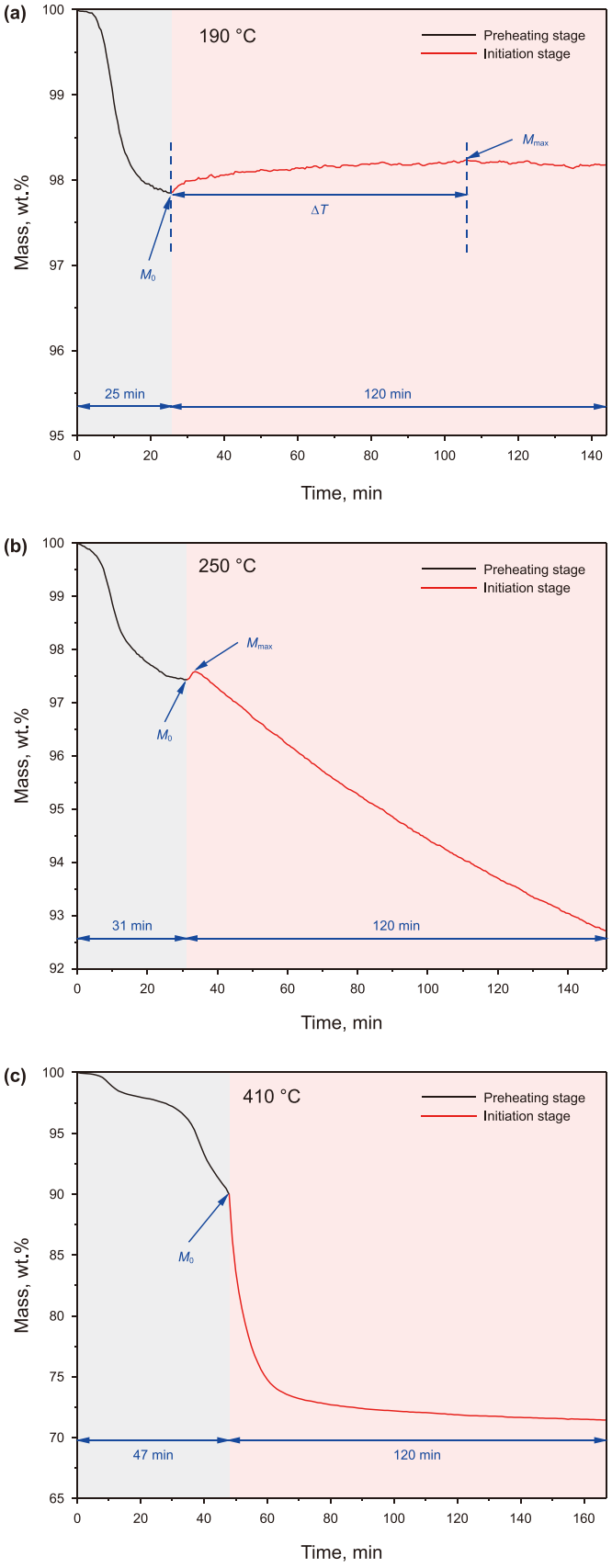

Fig. 3. The TG curves in 21% O_2/79% N_2 at **(a)** 190 °C, **(b)** 250 °C, and **(c)** 410 °C.

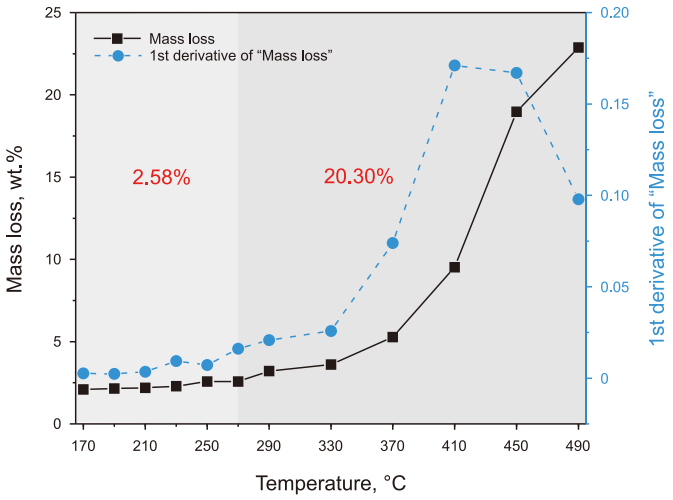

Fig. 4. The total mass loss and its first derivative of OS in the preheating stage at different temperatures.

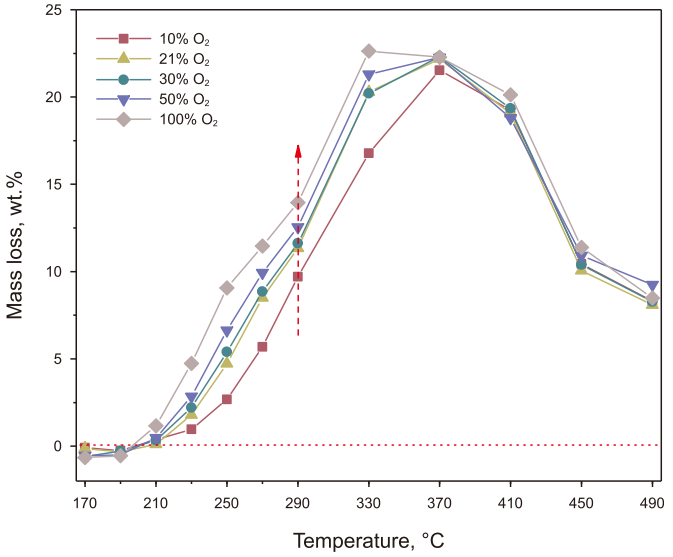

Fig. 5. The total mass loss of OS in the initiation stage at different initiation temperatures with various oxygen concentrations.

early stage. Then the decreasing rate slows down continuously and basically reaches a steady state after a certain temperature. When *a* is 30%, the time experienced decreases rapidly and starts to stabilize after 290 °C. While it basically starts to stabilize after 370 °C when *a* is 50% and 410 °C when *a* is 90%. This demonstrates that increasing the initiation temperature could greatly promote the cracking and oxidation reactions of organic matter, thus significantly shortening the reaction time. Furthermore, this promotion effect is more pronounced during the initial rise in temperature, while it considerably decreases after the temperature reached a specific level.

In addition, at the same initiation temperature, the time required to reach the target *a* basically shows a steady decrease with the increase in oxygen concentration, which suggests that higher oxygen concentrations can greatly promote reactions such as oxidation and pyrolysis in the initiation stage, thus increase the reaction rate. It is noteworthy that all three times in 10% O_2/90% N_2 are shorter at 210 °C, while they all increase when the temperature increases to 230 °C. Based on the results in Fig. 5, it is evident that at 210 °C, very little substance is able to take part in the reaction, while there is a significant increase when the temperature increases to 230 °C. The increased mass of reactants makes the reaction time increase. Similar phenomena are not observed when the oxygen concentration increases (21%, 30%, and 50%) or when the initiation temperature is higher (≥230 °C). This indicates that the increase in oxygen concentration or temperature promotes the oxidation and pyrolysis reactions, resulting in a constant decrease in the time experienced. In 100% O_2, the times corresponding to 30% and 50% decrease with temperature, while the time corresponding to 90% appears to increase from 210 to 230 °C. This indicates that in 100% O_2, more substances are involved in the reaction at the later stages of the reaction, prolonging the reaction time. This is also evidenced by the apparent increase in weight loss from 210 to 230 °C of 100% O_2 in Fig. 5. Moreover, the decreasing trend in time experienced shows a significant hysteresis in 290–330 °C and remains almost stable, which can be clearly seen in Fig. 6(b) and (c). This phenomenon indicates a significant deterioration of the oxygen initiation reaction properties of OS at 290–330 °C, which may be related to severe pore blockage caused by plenty of bitumen generated and the bitumen coking during the ignition; this is consistent with our previous studies (Xu et al., 2023a).

3.2. Isothermal kinetic analysis

3.2.1. Isothermal kinetic model

In order to investigate the reaction kinetic properties of the initiation stage, the classical "lnln" method was chosen to calculate the reaction activation energy of the isothermal initiation stage. According to the law of mass action, the reaction kinetic equation and the related calculation equation are as follows (Xu et al., 2023a):

Table 2
Maximum weight-gain through oxidation of OS at initiation stage and its corresponding time.

Temp., °C	10% O_2/90% N_2		21% O_2/79% N_2		30% O_2/70% N_2		50% O_2/50% N_2		100% O_2	
	Δ*M*, %	Δ*T*, min	Δ*M*, %	Δ*T*, min	Δ*M*, %	Δ*T*, min	Δ*M*, %	Δ*T*, min	Δ*M*, %	Δ*T*, min
170	0.11	112.5	0.27	111	0.62	112.5	0.65	111.5	0.67	118
190	0.28	94.5	0.39	81	0.39	61.5	0.55	58	0.74	54.5
210	0.16	23.5	0.34	19.5	0.35	18.5	0.42	15	0.54	11
230	0.16	17	0.21	7.5	0.27	5	0.31	5	0.37	3.5
250	0.11	3.5	0.15	2.5	0.16	2.5	0.18	2	0.23	1.5
270	0.10	2.5	0.09	1.5	0.07	1.5	0.10	1.5	0.13	1
290	0.09	1.5	0.04	1.5	0.05	1	0.05	1	0.06	1
330	0.07	1	0.02	1	0.05	1	–	–	–	–
370	–	–	–	–	–	–	–	–	–	–

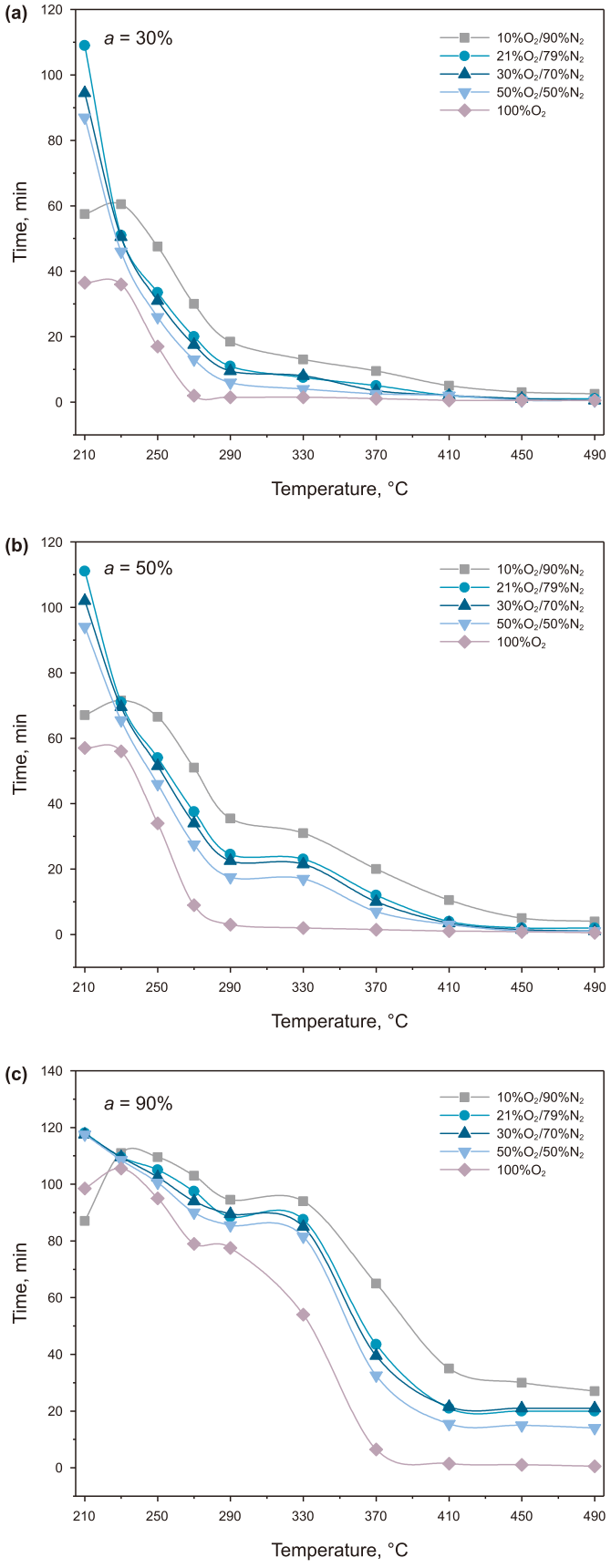

Fig. 6. Time experienced for the sample weight loss ratio, a (sample weight loss vs. total weight loss), to reach **(a)** 30%, **(b)** 50%, and **(c)** 90% during the initiation stage of various TG curves.

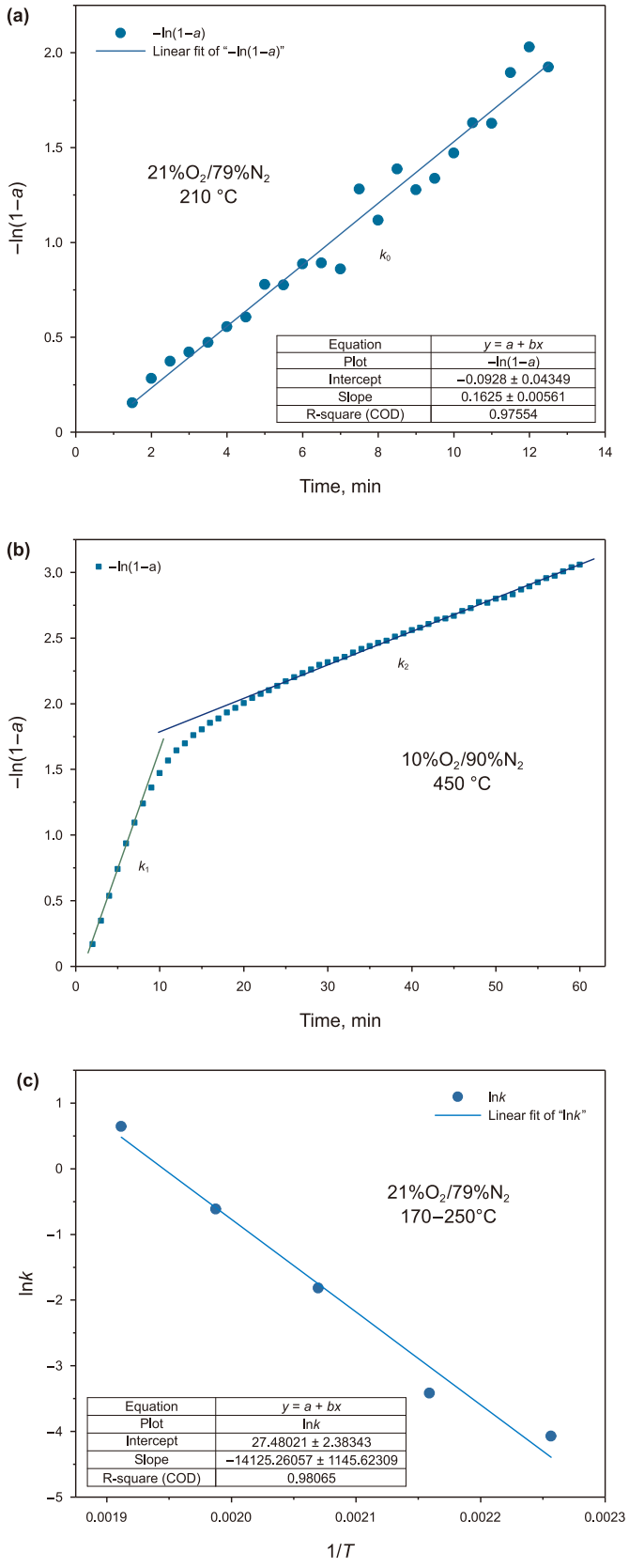

Fig. 7. Schematic diagram of the calculation process for the reaction activation energy in the isothermal initiation stage by the "lnln" method: **(a)** calculation process of the first step for the oxidative weight-gain phase; **(b)** calculation process of the first step for the oxidative reaction phase; **(c)** calculation process of the second step.

Table 3
Kinetic parameters related to the oxidative weight-gain phase of the OS isothermal OIP at different temperatures and gas mixtures.

Temp., °C	10% O_2/90% N_2		21% O_2/79% N_2		30% O_2/70% N_2		50% O_2/50% N_2		100% O_2	
	k_0	R^2	k_0	R^2	k_0	R^2	k_0	R^2	k_0	R^2
170	0.0012	0.90	0.0040	0.94	0.0206	0.98	0.0206	0.98	0.021	0.98
190	0.0046	0.91	0.0082	0.93	0.059	0.94	0.059	0.97	0.0634	0.96
210	0.0266	0.90	0.0338	0.97	0.2146	0.96	0.2146	0.96	0.3462	0.99
230	0.0758	0.96	0.0868	0.97	0.7658	0.98	0.8356	0.99	1.4712	0.97

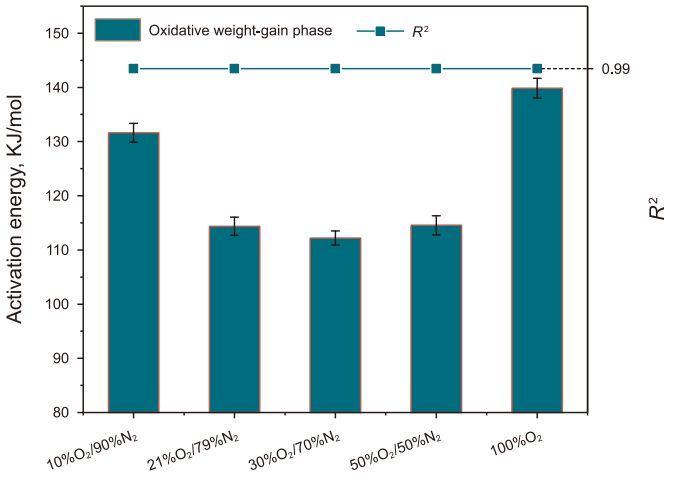

Fig. 8. Activation energies for the oxidative weight-gain phase of OS OIP under different gas mixtures.

$$a = \frac{\Delta m_t}{\Delta m_0} \tag{1}$$

$$\frac{da}{dt} = f(a)k \tag{2}$$

where, a is the conversion rate at t, which has the same meaning as the mass loss ratio in Fig. 6; Δm_t is the weight loss at t; Δm_0 is the total weight loss; t is the time; and $f(a)$ is the reaction mechanism function. Since the reaction of OS with oxygen is considered to be a primary reaction, assume $f(a)=(1-a)^n$ and the reaction energy level $n = 1$; k is the reaction rate constant.

By integrating both sides of Eq. (2) and substituting the boundary condition of $t = 0$, $a = 0$, the following equation can be obtained (Xia et al., 2011):

$$-\ln(1-a) = kt \tag{3}$$

Moreover, the Arrhenius equation can be used to get the following equation:

$$\ln k = \ln A - \frac{E}{RT_{\text{isothermal}}} \tag{4}$$

where, A is the pre-exponent factor, s^{-1}; E is the reaction activation energy, kJ/mol; R is the universal gas constant, 8.314 J mol^{-1} K^{-1}; $T_{\text{isothermal}}$ is the initiation temperature, °C.

The reaction rate constant k can be determined from the slope of the plot of $-\ln(1-a)$ vs. t. Subsequently, the values of E and A can be obtained from the slope and intercept of Eq. (4). Therefore, the activation energy of the isothermal oxygen initiation reaction of OS can be determined by the isothermal TG curve in a certain temperature range. The calculation processes are shown in Fig. 7.

3.2.2. The kinetic characteristics of oxidative weight-gain phase

Based on the analysis of the above behavior characteristics, the initiation stage was divided into two typical reaction phases: the oxidative weight-gain phase and the oxidative reaction phase. Due to the large quantity of oxidized groups produced by the oxygen addition reaction and the failure of subsequent reactions to occur at lower temperatures, the sample shows an obvious oxidative weight gain, which is recorded as the oxidative weight-gain phase. As the temperature increases, the generated oxidation groups as well as the remaining organic matter tend to undergo decomposition, isomerization, pyrolysis, and oxidative cracking reactions, resulting in large quantities of escaping gaseous products and the formation of fuel deposits such as residual carbon. Subsequently, these fuels undergo oxidative reactions, leading to a further decrease in sample mass, which is defined as the oxidative reaction phase.

Since the OIP of OS is a very complex chemical reaction process containing multiple parallel and overlapping reactions, there is no obvious reaction temperature boundary between these two stages. To better characterize the kinetic properties of these two stages, the main reaction temperature intervals corresponding to each stage were selected to be 170–230 °C for the oxidative weight-gain phase and 330–490 °C for the oxidative reaction phase, and the reaction activation energies were calculated for each stage, respectively. In the oxidative weight-gain phase, the parts between M_0 and $M_{\max}$ were selected to calculate the reaction activation energy of oxygen addition reaction. Table 3 and Fig. 8 show the relevant parameters and reaction activation energies of the oxidative weight-gain phase of the OS OIP at different temperatures and oxygen concentrations, respectively.

Table 3 suggests that the "lnln" method has a good fit to the data of the oxidative weight-gain phase of OS at 170–230 °C. The majority of R^2 is above 0.95, which proves the reliability of the fit results and the reaction stability of the oxidative weight-gain phase. Generally, an increase in the O_2 concentration, which is the reactant in the reaction process, contributes to the oxidation reaction. However, this also leads to an increase in the total amount of organic matter involved in the oxidation reaction, making more substances that are difficult to react with participate in the oxidation reaction, leading to an increase in the difficulty of the reaction (Bai et al., 2016; Zhao et al., 2024). Fig. 8 illustrates that with the increase in O_2 concentration, the activation energy shows a decreasing-increasing trend. When the O_2 concentration is increased from 10% to 21%, a significant decrease in activation energy occurs, from 131.63 to 114.37 kJ/mol, indicating that the increase in O_2 concentration can greatly promote the oxidation reaction and cause a significant decrease in activation energy. After that, a small decrease in activation energy occurs again as the O_2 concentration increased to 30%, indicating that the promotion effect of O_2 concentration is still dominant at this time. Nevertheless, the activation energy of the reaction starts to rise continuously with O_2 concentration and reaches a peak of 139.87 kJ/mol at 100% O_2. This result suggests that more substances that are difficult to react with participate in the oxidation reaction when the O_2 concentrations are 50% and 100%, leading to increases in the reaction

Table 4
Kinetic parameters related to the oxidative reaction phase of OS isothermal OIP at different temperatures and gas mixtures.

Temp., °C	10% O_2/90% N_2		21% O_2/79% N_2		30% O_2/70% N_2		50% O_2/50% N_2		100% O_2	
	k_1	R^2	k_1	R^2	k_1	R^2	k_1	R^2	k_1	R^2
330	0.0190	0.99	0.0214	0.99	0.0222	0.99	0.0218	0.99	0.9542	0.99
370	0.0346	0.99	0.0520	0.99	0.0568	0.99	0.0662	0.99	1.2532	0.99
410	0.0720	0.99	0.1285	0.99	0.1560	0.99	0.3374	0.99	1.4720	0.95
450	0.1447	0.99	0.3587	0.99	0.3912	0.95	0.7424	0.98	2.3744	0.99
490	0.2444	0.99	0.4863	0.96	0.6667	0.99	1.1669	0.99	3.0885	0.99
	k_2	R^2	k_2	R^2	k_2	R^2	k_2	R^2	k_2	R^2
330	0.0312	0.99	0.0288	0.99	0.0270	0.99	0.0268	0.99	0.0226	0.99
370	0.0396	0.99	0.0464	0.99	0.0466	0.99	0.0474	0.99	0.1170	0.99
410	0.0466	0.97	0.0607	0.94	0.0606	0.97	0.0706	0.98	0.7000	0.99
450	0.0602	0.95	0.0829	0.97	0.0872	0.99	0.0900	0.96	–	–
490	0.073	0.96	0.1001	0.99	–	–	–	–	–	–

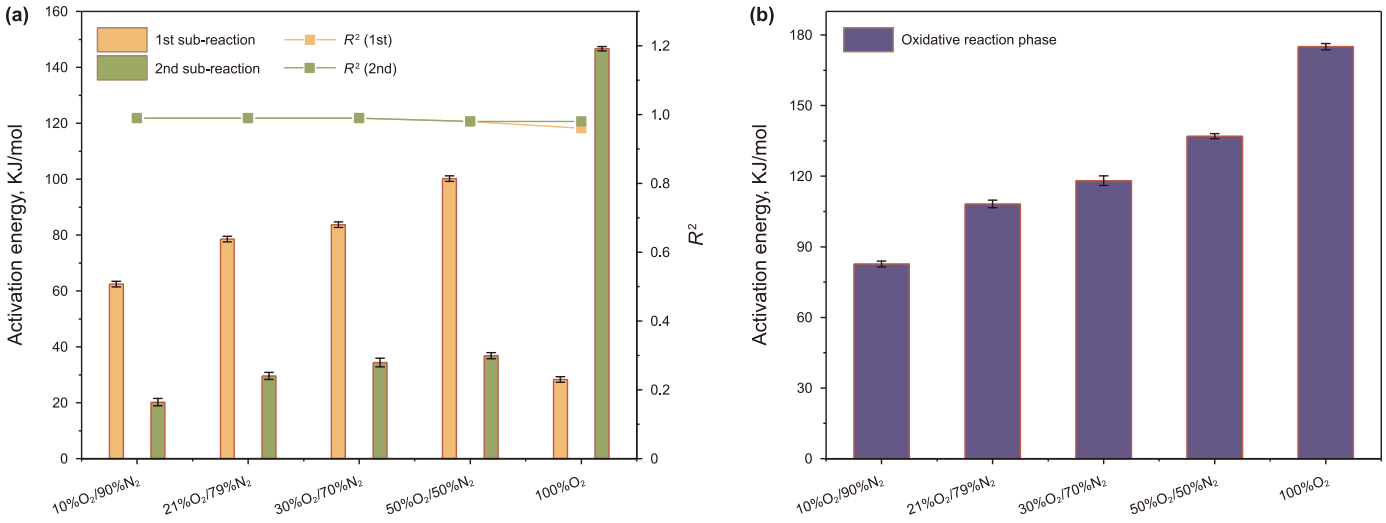

Fig. 9. Activation energies of **(a)** the first and second sub-reactions and **(b)** the total activation energy of the oxidative reaction phase of OS isothermal OIP under different gas mixtures.

difficulty and the activation energy. This phenomenon is most pronounced at 100% O_2.

3.2.3. The kinetic characteristics of oxidative reaction phase

Meanwhile, the activation energy was calculated by selecting the initiation stage data at 330–490 °C to evaluate the kinetic reaction characteristics of OS oxidation at oxidative reaction phase. As shown in Fig. 7(b), the first-step calculation results of the oxidative reaction phase show a clear two-stage feature, including two distinct slopes (k_1 and k_2), which indicates that the reaction is mainly proceeding in two sub-reactions. Therefore, the relevant kinetic parameters of these two sub-reactions were calculated, respectively, and the results are shown in Table 4 and Fig. 9. Due to the fast reaction rate at higher O_2 concentrations and temperatures, as well as the limited measurement accuracy of the TG apparatus, sufficient data could not be recorded for calculation at the later stages of the experiment. As a result, a few fit results are missing at 450 and 490 °C.

Similarly, as shown in Table 4, the "lnln" method also fits well for the two sub-reactions of the oxidative reaction phase at 330–490 °C. The R^2 basically all lies above 0.95, which proves the reliability of the fitting results and the reaction stability of the oxidative reaction phase. According to Fig. 9(a), the activation energy increases continuously with the increase in O_2 concentration but decreases abruptly at 100% O_2 in the first sub-reaction. While in the second sub-reaction, the activation energy first increases slowly with the increasing O_2 concentration and finally increases abruptly and significantly at 100% O_2. Based on the oxidative properties of bitumen and kerogen in OS reported in the relevant literature (Sun et al., 2014; Guo et al., 2016a; Ifticene et al., 2022; Xu et al., 2023b), the first sub-reaction is considered to be primarily the decomposition, isomerization, pyrolysis, and oxidative cracking of the generated oxidative groups as well as the remaining organic matter. This process generates a large amount of gaseous products that escape and form fuel deposits (e.g., residual carbon). And the second sub-reaction is mainly the oxidation of the generated fuel. As the O_2 concentration increases from 10% to 50%, the oxidation reaction is continuously enhanced, the rate is increased, and the reaction time is shortened (Fig. 6). Therefore, as the oxygen concentration increases, more substances are oxidized within the same time, and the exothermic peak will be higher (Fig. 10). This leads to an increase in reaction difficulty and activation energy. Finally, the excessive oxygen concentration in 100% O_2 leads to a large number of violent and rapid oxidation reactions. Substantial amounts of organic matter are directly used as fuel for the second sub-reaction. This leads to a significant reduction in reactants of first sub-reaction, which results in a significant decrease in its activation energy. In contrast, the second sub-reaction has a much higher amount of reactants and much higher activation energy.

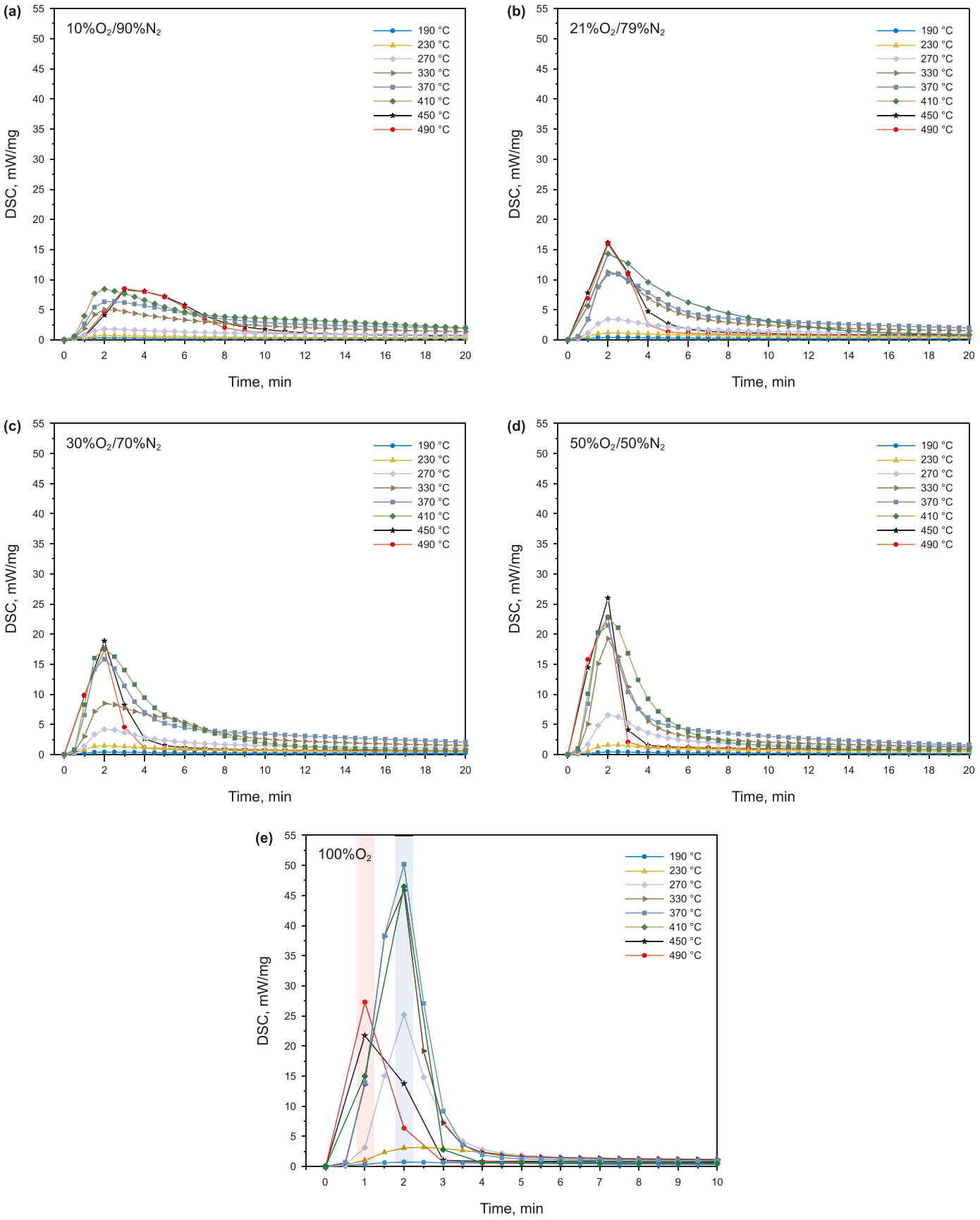

Fig. 10. DSC curves of the initiation stage in the OS isothermal OIP under **(a)** 10% O_2/90% N_2, **(b)** 21% O_2/79% N_2, **(c)** 30% O_2/70% N_2, **(d)** 50% O_2/50% N_2, and **(e)**100% O_2.

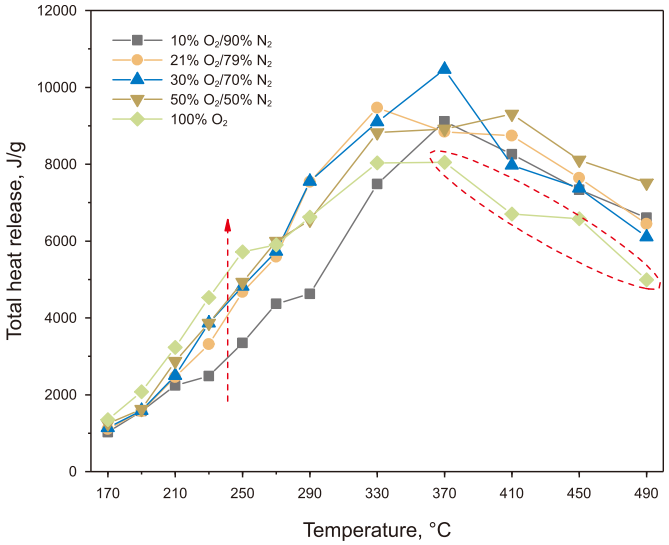

Fig. 11. Integration results of the DSC curves of the initiation stage (120 min) in the OS isothermal OIP under different gas mixtures.

3.3. The heat release characteristics during OIP

Fig. 10 shows the DSC curves of the initiation stage in the OS isothermal OIP under different gas mixtures. The results show that the reactions occurring at the initiation stage release a large amount of heat. With the increasing O_2 concentration, the exothermic peak increases significantly, and the required reaction time is shortened. This suggests that increasing the O_2 concentration can greatly promote the OIP process. In 10% O_2/90% N_2, the exothermic peak shows an increasing trend with the rising initiation temperature (190–490 °C), reaching a maximum at 490 °C. While the exothermic peak increases from 190 to 450 °C and starts decreasing after 450 °C in mixtures with 21%, 30%, and 50% O_2 concentrations. Similarly, the exothermic peak increases from 190 to 410 °C and begins to decrease after 410 °C in 100% O_2. The above phenomena indicate that the oxidative reaction of organic matter is less intense at lower O_2 concentrations. As the temperature increases, the hydrocarbon products released in the preheating stage increase, and the residual organic content decreases after entering the initiation stage (Figs. 4 and 5). However, the change in the residual organic content has little effect on the exothermic peak, suggesting that the O_2 concentration plays a major role at this point. In addition, the exothermic peaks at 450 and 490 °C are relatively lagging. Residual carbon is the main reactant in the initiation stage at these two temperatures, suggesting that oxidation of residual carbon is more difficult to occur. Overall, the oxidative reactions at lower O_2 concentrations are smooth and slow.

Afterwards, the reaction in the OIP process is continuously enhanced as the O_2 concentration increases to 21%, 30%, and 50%. The intensity of the oxidative exothermic reaction increases with temperature, with a maximum exothermic peak at 450 °C. A similar phenomenon is evident at 100% O_2, with a maximum at 370 °C. Following this, the exothermic peak continues to decrease due to the decrease in the residual organic matter content. This is generally consistent with the change in organic content during the initiation stage (Fig. 5), indicating that almost all organic matter is rapidly consumed at 100% O_2.

In addition, the exothermic peaks at 21%, 30%, and 50% O_2 occur at almost the same time. However, at 100% O_2, the exothermic peaks at 450 and 490 °C are significantly earlier, contrary to the 10% O_2 concentration. As shown in Fig. 10(e), at 1 min, the exothermic intensity increases with increasing temperature. After that, at 2 min, due to the decrease of the remaining organic matter, the exothermic intensity tends to increase and then decrease with the initiation temperature and reaches its maximum at 370 °C, which is basically the same as the change of weight loss in Fig. 5. These suggest that in 100% O_2, the residual carbon can be oxidized rapidly and violently when just entering the initiation stage, driving the reaction to a rapid exothermic peak.

The various DSC curves in the initiation stage with a reaction time of 120 min were integrated to obtain their total heat release, and the results are shown in Fig. 11. The results show that the total heat releases are basically consistent across different O_2 concentrations. First, the total heat releases increase with the rise of initiation temperature and reach its maximum at 330–370 °C, respectively, indicating that the rising initiation temperature can effectively increase the total amount of reactive substances. After that, due to the reduction in the amount of residual organic matter in the initiation stage, the total heat release show a decreasing trend.

Furthermore, the total heat release in 10% O_2/90% N_2 shows lower levels at 170–330 °C. Whereas, it shows the highest level at 170–250 °C in 100% O_2. In 21%, 30%, and 50% O_2 concentrations, the total heat release basically shows an increasing trend with the increasing O_2 concentration at lower temperatures. These demonstrate that the reaction property of organic matter in OS is greatly affected by the O_2 concentration at lower temperatures, and increasing the O_2 concentration can effectively promote the oxidative reaction of organic matter. Comparatively, the results for 100% O_2 show a lower total heat release at high temperatures, whereas the results for other O_2 concentrations are essentially at the same level. This is attributed to the rapid and intense oxidative-exothermic reaction of organic matter in 100% O_2, which has an extremely high O_2 concentration. Hence, a substantial amount of heat is released in a short period of time, which promotes the pyrolysis of kerogen and the generation and escape of partial hydrocarbon products, resulting in a decrease in the total reactants and heat release. In addition, the highest total heat release is obtained at 370 °C in 30% O_2/70% N_2, suggesting that a moderate combination of O_2 concentration and initiation temperature contributes to a better initiation effect. These should be considered during the construction of the OIP.

3.4. The product release characteristics during OIP

Fig. 12 shows the real-time infrared spectra of gas products in OS isothermal OIP in 10% O_2/90% N_2 at different initiation temperatures. Usually, the peaks located near 2850 and 2960 cm^{-1} in the infrared spectrum are the vibrational peaks of C–H bonds, which correspond to hydrocarbon products; the peaks located near 2350 and 667 cm^{-1} are the absorption peaks of CO_2. Since the switching from nitrogen to oxygenated atmosphere was designed during the experiment, the background of nitrogen atmosphere was used throughout the experiment. As shown in Fig. 12, the products in OIP are mainly hydrocarbon gas produced in the preheating stage and CO_2 produced in the initiation stage. With the increasing initiation temperature, the product peaks start to appear at 330 °C in the preheating stage and become obvious after 410 °C, suggesting that the oil and gas output starts to be produced in large quantities. While in the initiation stage, the corresponding peaks of CO_2 start to appear at 270 °C. After that, with the increasing initiation temperature, these two obvious CO_2 peaks are enhanced continuously, indicating that the CO_2 output becomes more and more intense, the corresponding reaction time becomes shorter, and the release becomes more concentrated.

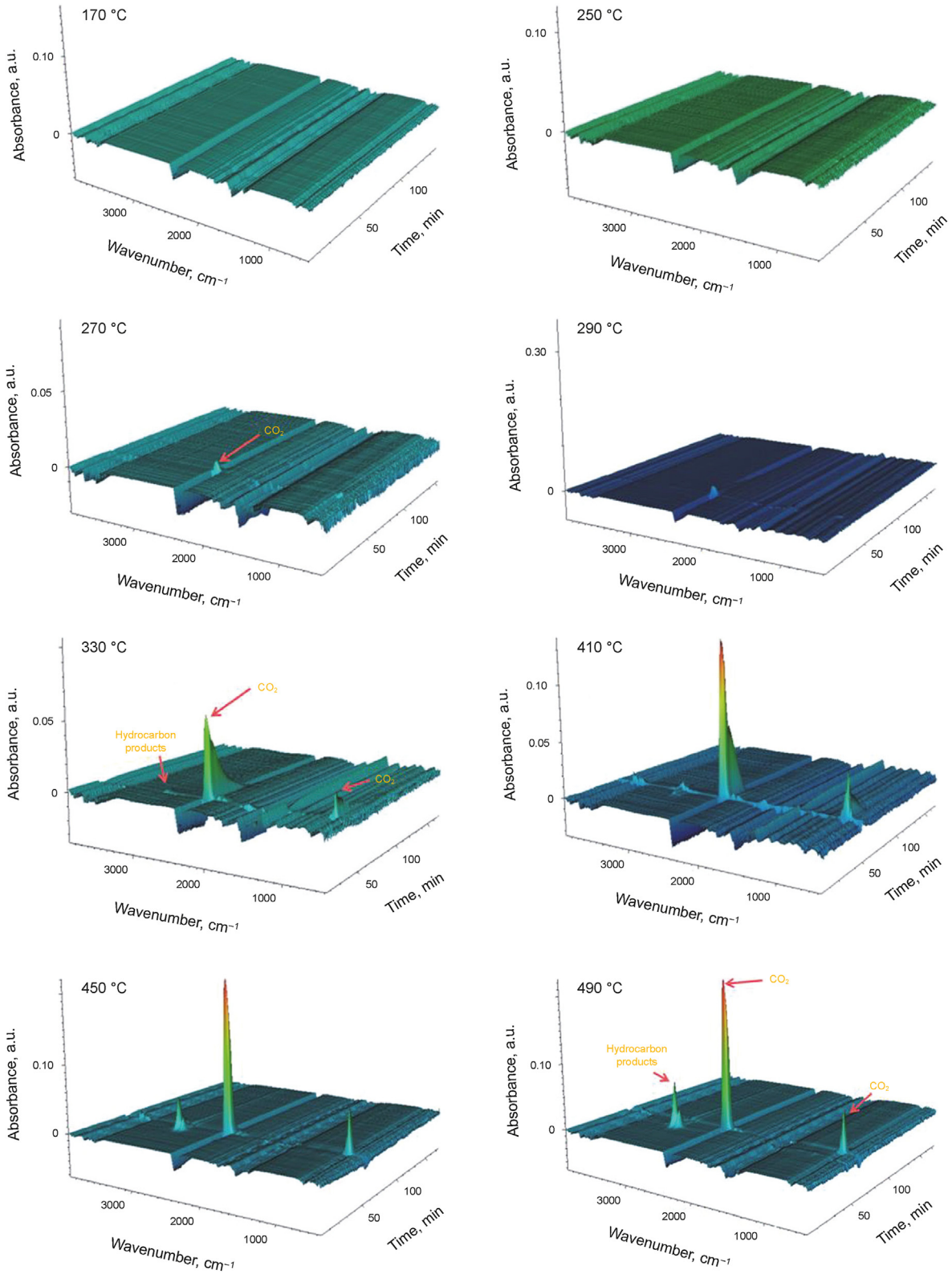

Fig. 12. Real-time infrared spectra of gas products in OS isothermal OIP under 10% O_2/90% N_2 at different initiation temperatures.

The IR spectra of OS near 667, 2350, 2850, and 2960 cm^{-1} at different temperatures in various atmospheres are shown in Fig. 13 and Figs. S1–S4. The results show that as oxygen concentration increases, the temperature corresponding to the initial production of CO_2 gradually decreases from 210 to 190 °C, with the corresponding peaks becoming sharper. Additionally, the point at which hydrocarbons begin formation drops from 330 to 250 °C. According to the aforementioned phenomenon, an increase in oxygen

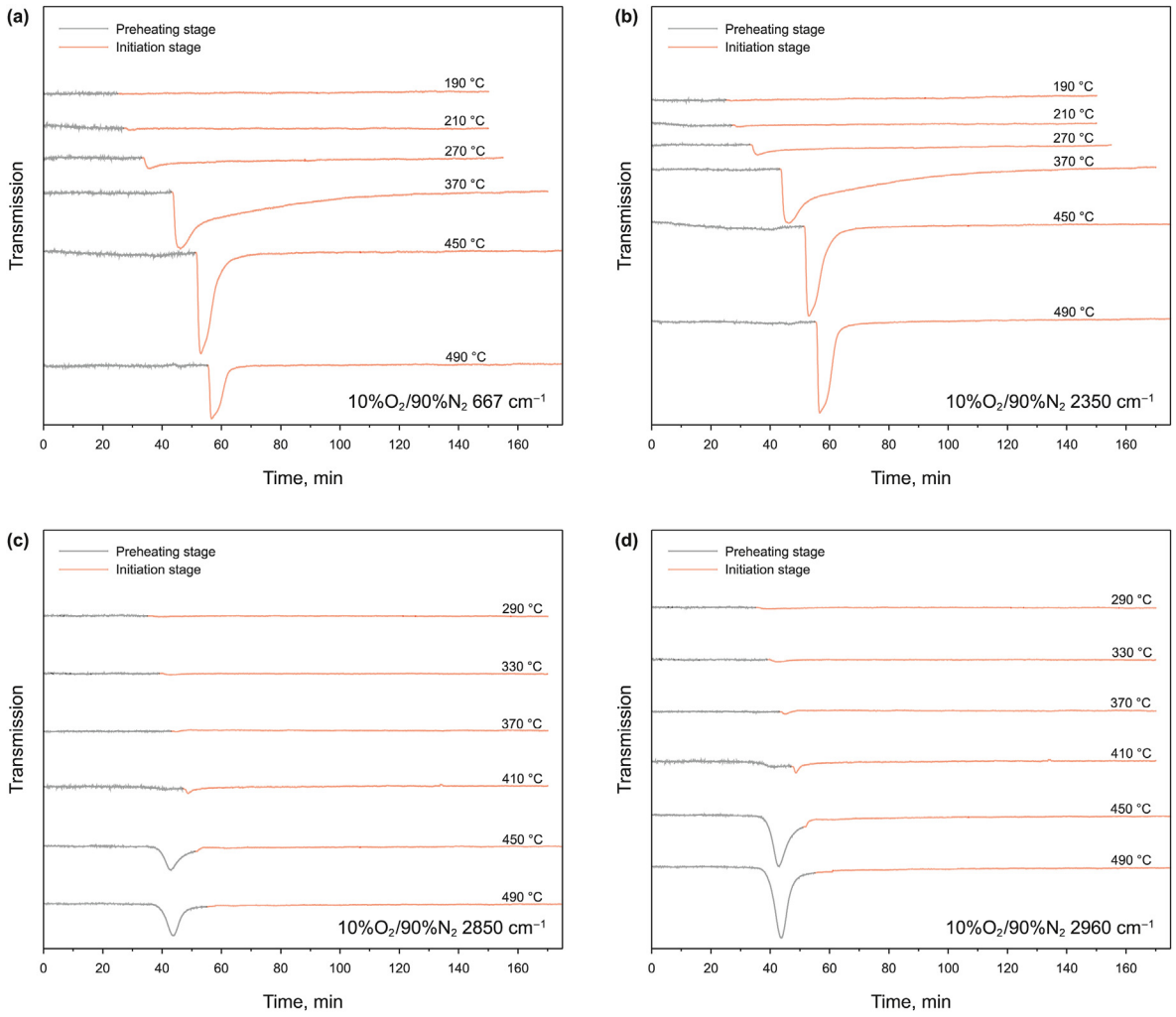

Fig. 13. IR spectra of OS near **(a)** 667, **(b)** 2350, **(c)** 2850, and **(d)** 2960 cm^{-1} in 10% O_2/90% N_2 at different temperatures during isothermal OIP.

concentration can speed up the oxidation reaction and enhance its intensity, which will then accelerate kerogen pyrolysis and the resulting generation of hydrocarbons. Furthermore, when oxygen is introduced at specified temperature intervals, especially at 410 °C, a noticeable rise in the intensity of hydrocarbon production could be noticed. And this is much more noticeable when the oxygen concentration is raised. It demonstrates that the oxidation and pyrolysis reactions happen simultaneously when oxygen is introduced, quickly completing the reaction. The reaction intensity intensifies and the reaction time constantly decreases as oxygen concentration increases.

3.5. Mechanism analysis of the OIP

Based on the above experimental results, the reaction mechanisms of OS in isothermal OIP under different initiation temperatures were discussed and schematically shown in Fig. 14. The results demonstrate that the isothermal OIP of OS is mainly controlled by the initiation temperature, and the reactions are mainly classified into three types: reactions (i), (ii), and (iii). First, when the initiation temperature is low (170–190 °C), the kerogen mainly undergoes an oxidative weight-gain reaction (I) without obvious mass loss and product generation, which is denoted as reaction (i). At this point, oxygen addition reactions primarily occur. The aliphatic hydrocarbon radicals (−R•), methyne (R3−CH), and aliphatic groups in kerogen will react with oxygen to form oxidized radicals including hydroxyl (−OH), carboxyl (−COOH), aldehyde (−CHO), and ether (−O−R) groups, resulting in an increase in mass (Fig. 5 and Table 2) and the release of a small amount of heat (Figs. 10 and 11) (Xu et al., 2023b). Whereas, due to the extremely low ambient temperature, these oxidized radicals are essentially unable to undergo further oxidation reactions, only a small decrease in sample mass from M_{max} occurs, and the final result still shows an increase.

At the initiation temperature of 210–290 °C, kerogen first undergoes an oxygen addition reaction to produce oxidized groups. Afterwards, these oxidizing groups and kerogen undergo further reactions such as decomposition, isomerization, pyrolysis, and oxidative cracking to produce fuel deposits such as residual carbon (condensed coke), which release large amounts of hydrocarbon products, CO_2, and heat (II_1). These fuels then undergo further oxidative reactions to be consumed, releasing CO_2 and large amounts of heat (II_2). The above reaction process is denoted as reaction (ii). However, at higher initiation temperatures (>330 °C), the oxidative weight gain reaction of kerogen is largely unobserved. High temperatures can greatly accelerate the oxidative reaction process, resulting in a rapid decrease in mass. As mentioned above, the oxidation reaction proceeds through two major sub-reactions. The OIP process at higher temperatures is referred to as reaction (iii).

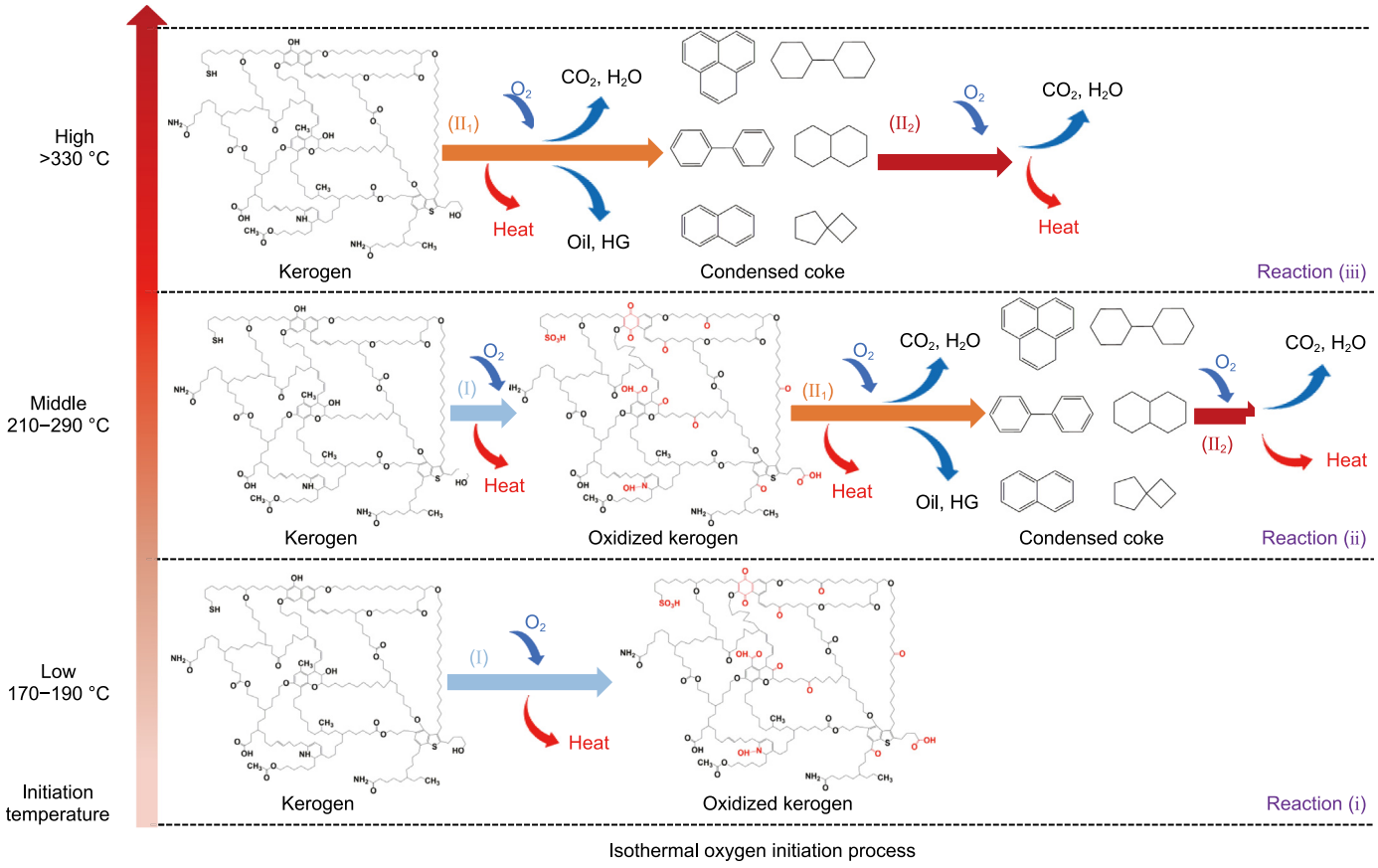

Fig. 14. Schematic diagram of the reaction mechanism for the OS isothermal OIP at different initiation temperatures (I: oxidative weight-gain reaction; II_1: the first sub-reaction of the oxidative reaction phase; II_2: the second sub-reaction of the oxidative reaction phase; HG: hydrocarbon gas; the molecular structure of kerogen in the Huadian OS was based on Ru et al. (2012)).

In addition, an increase in O_2 concentration promotes an increase in sample mass loss at each temperature, but with more complex effects in terms of reaction activation energy, heat generation, and product release characteristics. On the one hand, an increase of oxygen concentration can promote the occurrence of oxidation reaction, increase the reaction intensity, and shorten the reaction time. On the other hand, this can also make the amount of substances involved in the reaction increase, increasing the difficulty of the reaction and the reaction activation energy. Furthermore, very high oxygen concentrations at high temperatures promote the release of hydrocarbon products, resulting in a reduction of oxidized reactants, leading to a reduction in total heat release.

The above results are based on the isothermal oxygen-initiated TG/DSC-FTIR experiments in this study in order to investigate the OIP characteristics of OS at different constant temperatures. In fact, the temperature of the reaction zone in the actual OS exploitation process is constantly and dynamically changing as the reaction progresses. Therefore, it is necessary to adjust the initiation temperature and regulate the oxygen concentration to guide the production of the actual construction according to the reaction characteristics of OS under different conditions. For example, in the early stages of exploitation, the OS layer needs to be quickly heated to a higher temperature. Therefore, higher initiation temperatures (≥410 °C, according to Fig. 6(c)) and oxygen concentrations (30% and 50%, according to Figs. 8–10) should be used, where oxidative reactions can occur more readily and quickly and more heat can be released to heat the layer. Subsequently, when a chain reaction is formed, the oxygen concentration needs to be reduced (10% and 21%, according to Figs. 8–10) to lower the reaction and oxidative exothermic rates, thus slowing down the consumption of organic matter and ensuring more hydrocarbon products and higher recovery rates. In summary, the different technological parameters affecting the OIP need to be adjusted during the exploitation process to achieve better construction results and hydrocarbon recoveries.

4. Conclusions

Based on the isothermal oxygen-initiation TG/DSC-FTIR experiments, the isothermal oxygen initiation process of Huadian oil shale was characterized by analyzing the reaction behaviors, kinetic characteristics, heat and product release characteristics at different temperatures with various oxygen concentrations. The main conclusions obtained from the investigation are as follows: (1) As the initiation temperature increased, the OS showed three different reaction behaviors in the initiation stage, i.e., reactions occur (i) at 170–190 °C, (ii) at 210–290 °C, and (iii) at > 330 °C. (2) When oxygenated gas is initially injected, free bitumen and kerogen first undergo an oxygen addition reaction to form oxidized groups, resulting in a small temporary increase in organic mass, known as the oxidative weight-gain phase. Subsequently, these oxidized groups and kerogen undergo pyrolysis and oxidation reactions, resulting in a continuous decrease in sample mass, which is known as the oxidative reaction phase. (3) The oxidative reaction phase consists of two main sub-reactions whose activation energies are

strongly influenced by the oxygen concentration. The first sub-reaction occurs mainly as decomposition, pyrolysis, and oxidative cracking of oxidizing groups and kerogen, releasing large amounts of gaseous products and generating fuel deposits such as residual carbon. While the second sub-reaction is mainly the oxidation of fuel. (4) The increase in oxygen concentration can significantly promote the occurrence of oxidation reaction, enhance the reaction intensity, and increase the reaction rate. The total heat release increases with the increase in initiation temperature and reaches its maximum at 330–370 °C, respectively, which is mainly affected by the combination of oxygen concentration and residual organic matter content. (5) The products generated in the preheating stage are mainly hydrocarbon gases, which begin at 330 °C and become noticeable after 410 °C. While the main product generated in the initiation stage is CO_2, the output becomes more intense as the temperature increases. Moreover, the corresponding reaction time becomes shorter, resulting in a more concentrated release of products.

CRediT authorship contribution statement

Shao-Tao Xu: Writing – original draft, Methodology, Investigation, Data curation, Conceptualization. **Xiao-Shu Lü:** Supervision, Methodology. **Han Wang:** Software, Methodology, Formal analysis. **You-Hong Sun:** Supervision, Resources, Funding acquisition, Conceptualization. **Shi-Jie Kang:** Methodology. **Zhen-Dong Wang:** Supervision. **Wei Guo:** Supervision, Funding acquisition. **Sun-Hua Deng:** Writing – review & editing, Supervision, Methodology, Conceptualization.

Declaration of competing interest

The authors declare that they have no known competing financial interests or personal relationships that could have appeared to influence the work reported in this paper.

Acknowledgements

This work was supported by the China Postdoctoral Science Foundation under Grant Number 2023M743305, the National Funding Program for Postdoctoral Fellows (GZC20232484), the National Key R&D Program of China (No. 2019YFA0705502, 2019YFA0705501), the Young and Middle-aged Excellent Team Project for Scientific and Technological Innovation of Jilin Province, China, and the National Natural Science Foundation of China (42202345).

Appendix A. Supplementary data

Supplementary data to this article can be found online at https://doi.org/10.1016/j.petsci.2024.07.024.

References

Amer, M.W., Alhesan, J.S.A., Marshall, M., et al., 2022. Energy efficient method of supercritical extraction of oil from oil shale. Energy Convers. Manag. 252, 115108. https://doi.org/10.1016/j.enconman.2021.115108.

Bai, F., Guo, W., Lü, X., et al., 2015a. Kinetic study on the pyrolysis behavior of Huadian oil shale via non-isothermal thermogravimetric data. Fuel 146, 111–118. https://doi.org/10.1016/j.fuel.2014.12.073.

Bai, F., Liu, Y., Lai, C., 2020a. Thermal degradations and processes of four k-erogens via thermogravimetric-fourier-transform infrared: pyrolysis performances, products, and kinetics. Energy & fuels 34 (3), 2969–2979. https://doi.org/10.1021/acs.energyfuels.9b04231.

Bai, F., Sun, Y., Liu, Y., 2016. Thermogravimetric analysis of Huadian oil shale combustion at different oxygen concentrations. Energy & Fuels 30 (6), 4450–4456. https://doi.org/10.1021/acs.energyfuels.5b02888.

Bai, F., Sun, Y., Liu, Y., et al., 2020b. Characteristics and kinetics of Huadian oil shale pyrolysis via non-isothermal thermogravimetric and gray relational analysis. Combustion Science and Technology 192 (3), 471–485. https://doi.org/10.1080/00102202.2019.1576650.

Bai, F., Sun, Y., Liu, Y., et al., 2015b. Thermal and kinetic characteristics of pyrolysis and combustion of three oil shales. Energy Convers. Manag. 97, 374–381. https://doi.org/10.1016/j.enconman.2015.03.007.

Bai, F., Zhao, J., Liu, Y., 2019. An investigation into the characteristics and kinetics of oil shale oxy-fuel combustion by thermogravimetric analysis. Oil Shale 36 (1), 1–18. https://doi.org/10.3176/oil.2019.1.01.

Bolotov, A.V., Yuan, C., Varfolomeev, M.A., et al., 2023. In-situ combustion technique for developing fractured low permeable oil shale: experimental evidence for synthetic oil generation and successful propagation of combustion front. Fuel 344, 127995. https://doi.org/10.1016/j.fuel.2023.127995.

Dyni, J.R., 2006. Geology and Resources of some world oil-shale deposits, vol. 5294. Scientific Investigations Report. https://doi.org/10.3133/sir29955294.

Guo, H., Cheng, Q., Jin, Z., et al., 2016a. Thermochemical processing of fuels involving the use of molecular oxygen. RSC Adv. 6 (104), 102231–102248. https://doi.org/10.1039/c6ra18616e.

Guo, H., Cheng, Q., Wang, D., et al., 2016b. Analyzing the contribution of semicokes to forming self-heating in the oil-shale self-heating retorting process. Energy & fuels 30 (7), 5355–5362. https://doi.org/10.1021/acs.energyfuels.6b00351.

Guo, H., Pei, Y., Wang, K., et al., 2015a. Identifying the reaction mechanism of oil-shale self-heating retorting by thermal analysis techniques. Fuel 160, 255–264. https://doi.org/10.1016/j.fuel.2015.07.106.

Guo, H., Yang, Y., Wang, K., et al., 2015b. Strengthening the applicability of self-heating retorting process to oil shale via co-retorting. Fuel 143, 1–8. https://doi.org/10.1016/j.fuel.2014.11.009.

Guo, W., Li, Q., Deng, S., et al., 2022a. Mechanism and reservoir simulation study of the autothermic pyrolysis in-situ conversion process for oil shale recovery. Petrol. Sci. 20 (2), 1053–1067. https://doi.org/10.1016/j.petsci.2022.08.030.

Guo, H., Peng, S., Lin, J., et al., 2013. Retorting oil shale by a self-heating route. Energy & Fuels 27, 2445–2451. https://doi.org/10.1021/ef4000424.

Guo, W., Yang, Q., Sun, Y., et al., 2020. Characteristics of low temperature co-current oxidizing pyrolysis of Huadian oil shale. J. Anal. Appl. Pyrol. 146, 104759. https://doi.org/10.1016/j.jaap.2019.104759.

Guo, W., Yang, Q., Zhang, X., et al., 2021. Thermal behavior of oil shale pyrolysis under low-temperature co-current oxidizing conditions. ACS Omega 6 (28), 18074–18083. https://doi.org/10.1021/acsomega.1c01875.

Guo, W., Zhang, X., Deng, S., et al., 2022b. Enhanced pyrolysis of Huadian oil shale at high temperature in the presence of water and air atmosphere. J. Petrol. Sci. Eng. 215, 110623. https://doi.org/10.1016/j.petrol.2022.110623.

He, L., Ma, Y., Yue, C., et al., 2020. Kinetic modeling of Kukersite oil shale pyrolysis with thermal bitumen as an intermediate. Fuel 279, 118371. https://doi.org/10.1016/j.fuel.2020.118371.

He, W., Sun, Y., Guo, W., et al., 2021. Controlling the in-situ conversion proc-ess of oil shale via geochemical methods: a case study on the Fuyu oil shale, China. Fuel Process. Technol. 219, 106876. https://doi.org/10.1016/j.fuproc.2021.106876.

Hrayshat, E.S., 2008. Oil shale-an alternative energy source for Jordan. Energy Sources, Part A Recovery, Util. Environ. Eff. 30 (20), 1915–1920. https://doi.org/10.1080/15567030701468175.

Huang, H., Yu, H., Xu, W., et al., 2023. A coupled thermo-hydro-mechanical-chemical model for production performance of oil shale reservoirs during in-situ conversion process. Energy 268, 126700. https://doi.org/10.1016/j.energy.2023.126700.

Ifticene, M., Yuan, C., Al-Muntaser, A., et al., 2022. Behavior and kinetics of the conversion/combustion of oil shale and its components under air condition. Fuel 324, 124597. https://doi.org/10.1016/j.fuel.2022.124597.

Jarosław, K., Alicja, K.N., Krzysztof, G., 2021. The criticality of crude oil for energy security: a case of Poland. Energy 220, 119707. https://doi.org/10.1016/j.energy.2020.119707.

Kang, S., Sun, Y., Deng, S., et al., 2021. Extraction of Huadian oil shale in subcritical $FeCl_2$ solution. Fuel Process. Technol. 211, 106571. https://doi.org/10.1016/j.fuproc.2020.106571.

Kang, S., Zhang, S., Wang, Z., et al., 2023. Highly efficient catalytic pyrolysis of oil shale by $CaCl_2$ in subcritical water. Energy 274, 127343. https://doi.org/10.1016/j.energy.2023.127343.

Kang, Z., Zhao, Y., Yang, D., 2020. Review of oil shale in-situ conversion technology. Appl. Energy 269, 115121. https://doi.org/10.1016/j.apenergy.2020.115121.

Kuang, W., Lu, M., Yeboah, I., et al., 2019. A comprehensive kinetics study on non-isothermal pyrolysis of kerogen from Green River oil shale. Chem. Eng. J. 377, 120275. https://doi.org/10.1016/j.cej.2018.10.212.

Li, J., Shan, X., Song, X., et al., 2022. Evaluation of the organic matter product of Huadian oil shale during pyrolysis using multiple approaches: guidance for the in situ conversion of oil shale. J. Anal. Appl. Pyrol. 167, 105656. https://doi.org/10.1016/j.jaap.2022.105656.

Liu, Z., Meng, Q., Dong, Q., et al., 2017. Characteristics and resource potential of oil shale in China. Oil Shale 34 (1), 15–41. https://doi.org/10.3176/oil.2017.1.02.

Martins, M.F., Salvador, S., Thovert, J.F., et al., 2010a. Co-current combustion of oil shale-Part 1: characterization of the solid and gaseous products. Fuel 89, 144–151. https://doi.org/10.1016/j.fuel.2009.06.036.

Martins, M.F., Salvador, S., Thovert, J.F., et al., 2010b. Co-current combustion of oil shale—Part 2: structure of the combustion front. Fuel 89 (1), 133–143. https://doi.org/10.1016/j.fuel.2009.06.040.

Mohammad, A.H., Omar, A.A., John, R., et al., 2011. Effect of demineralization and heating rate on the pyrolysis kinetics of Jordanian oil shales. Fuel Process.

Technol. 92 (9), 1805–1811. https://doi.org/10.1016/j.fuproc.2011.04.037.
Pan, L., Dai, F., Pei, S., et al., 2021. Influence of particle size and temperature on the yield and composition of products from the pyrolysis of Jimsar (China) oil shale. J. Anal. Appl. Pyrol. 157, 105211. https://doi.org/10.1016/j.jaap.2021.105211.
Raul, A.B., 2018. Fossil fuels, alternative energy and economic growth. Econ. Modell. 75, 196–220. https://doi.org/10.1016/j.econmod.2018.06.019.
Ru, X., Cheng, Z., Song, L., et al., 2012. Experimental and computational studies on the average molecular structure of Chinese Huadian oil shale kerogen. J. Mol. Struct. 1030, 10–18. https://doi.org/10.1016/j.molstruc.2012.07.027.
Saif, T., Lin, Q., Butcher, A., et al., 2017. Multi-scale multi-dimensional microstructure imaging of oil shale pyrolysis using X-ray micro-tomography, automated ultra-high resolution SEM, MAPS Mineralogy and FIB-SEM. Appl. Energy 202, 628–647. https://doi.org/10.1016/j.apenergy.2017.05.039.
Shi, Y., Zhang, Y., Song, X., et al., 2023. Injection energy utilization efficiency and production performance of oil shale in-situ exploitation. Energy 263, 125714. https://doi.org/10.1016/j.energy.2022.125714.
Song, X., Zhang, C., Shi, Y., et al., 2019. Production performance of oil shale in-situ conversion with multilateral wells. Energy 189, 116145. https://doi.org/10.1016/j.energy.2019.116145.
Sun, Y., Bai, F., Liu, B., et al., 2014. Characterization of the oil shale products derived via topochemical reaction method. Fuel 115, 338–346. https://doi.org/10.1016/j.fuel.2013.07.029.
Sun, Y., Guo, W., Deng, S., 2021a. The status and development trend of in-situ conversion and drilling exploitation technology for oil shale. Explor. Eng. 48 (1), 57–67. https://doi.org/10.12143/j.ztgc.2021.01.008 (in Chinese).
Sun, Y., Kang, S., Wang, S., et al., 2019. Subcritical water extraction of Huadian oil shale at 300 °C. Energy & Fuels 33 (3), 2106–2114. https://doi.org/10.1021/acs.energyfuels.8b04431.
Sun, Y., Xu, S., Yang, Q., et al., 2021b. Oxidizing pyrolysis of Huadian oil shale and its product distribution. J. China Univ. Pet. (Edition of Natural Science) 45 (2), 149–156. https://doi.org/10.3969/j.issn.1673-5005.2021.02.018 (in Chinese).
Wang, D., Liu, Y., Zhang, T., et al., 2021. Structural and quantitative evolution of organic matters in oil shale during two different retorting processes. AIChE J. 67 (8), 17278. https://doi.org/10.1002/aic.17278.
Wang, G., Liu, S., Yang, D., et al., 2022. Numerical study on the in-situ pyrolysis process of steeply dipping oil shale deposits by injecting superheated water steam: a case study on Jimsar oil shale in Xinjiang, China. Energy 239, 122182. https://doi.org/10.1016/j.energy.2021.122182.
Xia, Y., Xue, H., Wang, H., et al., 2011. Kinetics of isothermal and non-isothermal pyrolysis of oil shale. Oil Shale 28, 415. https://doi.org/10.3176/oil.2011.3.05.
Xu, S., Lü, X., Sun, Y., et al., 2023a. Optimization of temperature parameters for the autothermic pyrolysis in-situ conversion process of oil shale. Energy 264, 126309. https://doi.org/10.1016/j.energy.2022.126309.
Xu, S., Sun, Y., Guo, W., et al., 2023b. Regulating the oxidative assisted pyrolysis of Huadian oil shale by preheating temperature and oxygen flow rate. Energy 262, 125602. https://doi.org/10.1016/j.energy.2022.125602.
Xu, S., Sun, Y., Lü, X., et al., 2021. Effects of composition and pore evolution on thermophysical properties of Huadian oil shale in retorting and oxidizing pyrolysis. Fuel 305, 121565. https://doi.org/10.1016/j.fuel.2021.121565.
Xu, S., Sun, Y., Yang, Q., et al., 2023c. Product migration and regional reaction characteristics in the autothermic pyrolysis in-situ conversion process of low-permeability Huadian oil shale core. Energy 283, 128525. https://doi.org/10.1016/j.energy.2023.128525.
Xu, W., Shan, X., Yi, J., et al., 2023. Evolution of organic carbon isotopes during the pyrolysis of Nong'an oil shale in Songliao Basin and its implications for in-situ conversion project. Geomech. Geophys. Geo-energ. Geo-resour. 9 (1), 65. https://doi.org/10.1007/s40948-023-00616-1.
Yuan, C., Emelianov, D., Varfolomeev, M., et al., 2018. Oxidation behavior and kinetics of light, medium, and heavy crude oils characterized by thermogravimetry coupled with fourier transform infrared spectroscopy. Energy & Fuels 32 (4), 5571–5580. https://doi.org/10.1021/acs.energyfuels.8b00428.
Yuan, C., Emelianov, D., Varfolomeev, M., et al., 2019. Comparison of oxidation behavior of linear and branched alkanes. Fuel Process. Technol. 188, 203–211. https://doi.org/10.1016/j.fuproc.2019.02.025.
Yuan, C., Pu, W., Ifticene, M., et al., 2022. Crude oil oxidation in an air injection based enhanced oil recovery process: chemical reaction mechanism and catalysis. Energy & Fuels 36 (10), 5209–5227. https://doi.org/10.1021/acs.energyfuels.2c01146.
Yang, Q., Guo, M., Guo, W., 2021. Effects of associated minerals on the co-current oxidizing pyrolysis of oil shale in a low-temperature stage. ACS Omega 6 (37), 23988–23997. https://doi.org/10.1021/acsomega.1c03098.
Yang, Q., Zhang, X., Xu, S., et al., 2022. Low-temperature co-current oxidizing pyrolysis of oil shale: study on the physicochemical properties, reactivity and exothermic characters of semi-coke as heat generation donor. J. Petrol. Sci. Eng. 216, 110726. https://doi.org/10.1016/j.petrol.2022.110726.
Zhan, H., Yang, Q., Qin, F., et al., 2022. Comprehensive preparation and mult-iscale characterization of kerogen in oil shale. Energy 252, 124005. https://doi.org/10.1016/j.energy.2022.124005.
Zhao, S., Pu, W., Li, Y., et al., 2024. Oxidation behavior and kinetics of shale oil under different oxygen concentrations. Fuel 361, 130677. https://doi.org/10.1016/j.fuel.2023.130677.
Zhu, C., Guo, W., Sun, Y., et al., 2022. Reaction mechanism and reservoir simulation study of the high-temperature nitrogen injection in-situ oil shale process: a case study in Songliao Basin, China. Fuel 316, 123164. https://doi.org/10.1016/j.fuel.2022.123164.